NANO · MICRO small
www.small-journal.com

# Interfacial Engineering of Hierarchical Transition Metal Oxide Heterostructures for Highly Sensitive Sensing of Hydrogen Peroxide

*Wen Zhang, Guozheng Fan, Huan Yi, Gan Jia, Zhaosheng Li,* Chunwei Yuan, Yunfei Bai, and Degang Fu**

**Hydrogen peroxide ($H_2O_2$) is a major messenger molecule in cellular signal transduction. Direct detection of $H_2O_2$ in complex environments provides the capability to illuminate its various biological functions. With this in mind, a novel electrochemical approach is here proposed by integrating a series of CoO nanostructures on CuO backbone at electrode interfaces. High-resolution transmission electron microscopy (HRTEM), X-ray diffraction, and X-ray photoelectron spectroscopy demonstrate successful formation of core–shell CuO–CoO hetero-nanostructures. Theoretical calculations further confirm energy-favorable adsorption of $H_2O_2$ on surface sites of CuO–CoO heterostructures. Contributing to the efficient electron transfer path and enhanced capture of $H_2O_2$ in the unique leaf-like CuO–CoO hierarchical 3D interface, an optimal biosensor-based CuO–CoO-2.5 h electrode exhibits an ultrahigh sensitivity (6349 μA m $M^{-1}$ $cm^{-2}$), excellent selectivity, and a wide detection range for $H_2O_2$, and is capable of monitoring endogenous $H_2O_2$ derived from human lung carcinoma cells A549. The synergistic effects for enhanced $H_2O_2$ adsorption in integrated CuO–CoO nanostructures and performance of the sensor suggest a potential for exploring pathological and physiological roles of reactive oxygen species like $H_2O_2$ in biological systems.**

## 1. Introduction

Hydrogen peroxide ($H_2O_2$) is an important reactive oxygen species (ROS) generated from most oxidases in mitochondria, and plays essential functions in signal transduction of living cells.[1,2] The level of $H_2O_2$ can be served as a valuable biomarker of various bodily disorders such as Alzheimer's disease, cancer, diabetes, and neurodegeneration.[3–6] The capability of rapid and sensitive $H_2O_2$ detection could facilitate earlier diagnosis and clinical treatment of preventive and therapeutic strategies.[7,8] Furthermore, $H_2O_2$ also acts as a vital role in pharmaceutical, food, environmental, and cosmetic industries.[9,10] However, the consumption of excess $H_2O_2$ could cause skin irritation and damage to the upper gastrointestinal tract.[11] Therefore, development of an efficient sensor for $H_2O_2$ in biological environments is of urgency.

Several measurement techniques, such as spectrometry, fluorometry, colorimetry, chemiluminescence, and electrochemical analysis have been applied for monitoring $H_2O_2$.[12,13] Among these methods, electrochemical technique has drawn much attention for in situ and real-time detection for good selectivity, high sensitivity, and fast response.[14] In the past decades, enzyme-based electrochemical sensors have achieved great progress due to their high sensitivity and selectivity. However, enzyme may easily lose their biological activity by denaturation.[15,16] Therefore, enormous efforts have been paid on developing efficient nonenzymatic biosensors with high performance and excellent stability.[17] For developing nonenzymatic electrochemical sensors, various functional materials and nanostructures have been efficiently applied,[18–21] in which transition metal oxides, e.g., copper oxide, manganese dioxide, cobalt oxide, and iron oxide, have been utilized to catalyze $H_2O_2$ decomposition.[22]

Regarding sensing application, controllable preparation of 3D hierarchical nanostructures is ideal for obtaining excellent performance.[23,24] Rational design of efficient 3D interfaces benefited from studies on the interplay of nanostructure and material properties, provides chances to take full advantage in developing advanced biological and medical applications.[25–29] Recently, researches focus on exploitation of hierarchical 3D nanostructures (e.g., boxes, stars, spheres, flowers, cubes, etc.) from self-assembly of low dimensional building blocks, i.e., nanoparticles, nanowires, nanoribbons, etc.,[30–33] which possess porous structure with a large specific surface area, leading to their potency in catalysis, electroanalysis, fuel cells, sensors, and adsorption applications.[34,35]

W. Zhang, H. Yi, Prof. C. Yuan, Prof. Y. Bai, Prof. D. Fu
State Key Laboratory of Bioelectronics
Demonstration Center for Experimental Biomedical Engineering Education (Southeast University)
College of Biological Science and Medical Engineering
Southeast University
Nanjing 210096, P. R. China
E-mail: fudegang@seu.edu.cn
G. Fan, G. Jia, Prof. Z. Li
College of Engineering and Applied Sciences
Nanjing University
Nanjing 210093, P. R. China
E-mail: zsli@nju.edu.cn

DOI: 10.1002/smll.201703713

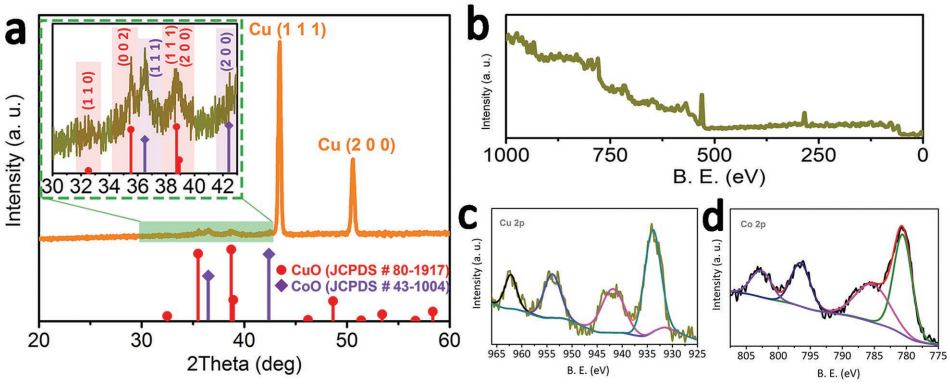


**Figure 1.** a) XRD pattern of CuO–CoO-2.5 h sample, inset shows the amplified view. b) XPS survey spectra, and high resolution spectra for c) Cu 2p and d) Co 2p.

Herein, we present a synthetic route to construct hierarchical CuO–CoO 3D interface over the copper foam electrode for $H_2O_2$ sensing via a controllable chemical bath deposition (CBD) process and subsequent calcination in inert atmosphere. The delicate hetero-nanostructures composed of porous CuO nanoplates as the core together with decorated CoO shell present a synergic effect, leading to enhancement in conductivity and adsorption, thus improving catalytic activity. Meanwhile, the effect of reaction time on the morphology and electrocatalytic performance was examined in detail. The sample CuO–CoO-2.5 h with leaf-like nanostructure achieved excellent electrochemical activity for $H_2O_2$ reduction, and exhibited promising sensing ability for $H_2O_2$ detection in real samples from juice and serum.

## 2. Results and Discussion

Crystal phases of CuO–CoO-*x* samples were examined by X-ray diffraction (XRD) patterns (**Figure 1**a and Figure S1 (Supporting Information)). As shown in Figure 1a, two strong peaks centered at 43.4° and 50.5° were corresponding to Cu (111) and (200) planes, respectively, which indicated the Cu foam substrate. Two typical diffraction peaks at 36.5° and 42.4° were well indexed to the (111) and (200) planes of cubic CoO (JCPDS # 43-1004), and the other four diffraction peaks located at 32.5°, 35.5°, 38.7°, and 38.9° were corresponding to standard monoclinic CuO (JCPDS # 80-1917). These results confirmed successful formation of CuO–CoO composite structure. The chemical states of as-prepared CuO–CoO-*x* samples were further characterized by X-ray photoelectron spectroscopy (XPS). The XPS spectra (Figure 1b and Figures S2–S4 (Supporting Information)) verified that CuO–CoO-*x* mainly contained cobalt, copper, and oxygen elements. The four peaks located at 934.1, 941.8, 953.8, and 962.3 eV (Figure 1c) can be assigned to Cu $2p_{3/2}$ and Cu $2p_{1/2}$ of Cu(II) and their satellites, respectively,[36] while the peaks centered at about 780.7, 785.9, 796.5, and 802.8 eV (Figure 1d) corresponding to Co $2p_{2/3}$, Co $2p_{1/2}$ of Co(II), respectively.[37] The high resolution XPS spectra of Cu and Co elements demonstrated existence of Cu(II) and Co(II) in the CuO/CoO heterostructures.

**Figure 2**a and Figure S5 (Supporting Information) illustrated the fabrication process of hybrid CuO–CoO-*x* core–shell hetero-nanostructures based on observation of scanning electron microscopy and transmission electron microscopy (TEM). First, porous $Cu(OH)_2$ plates (Figure S6, Supporting Information) were directly formed on Cu foam as backbone by simultaneous solution oxidation and precipitation processes. Then CBD method was used to obtain $Cu(OH)_2$–Co precursor/Cu foam composite that $Cu(OH)_2$/Cu foam was immersed into a solution containing urea and cobalt salts with different reaction times (2–3.5 h). Finally, the $Cu(OH)_2$–Co precursor/Cu foam was calcined under a $N_2$ atmosphere and converted into a 3D porous electrode with hierarchical interface of hybrid CuO–CoO core/shell nanostructures. The CuO–CoO-*x* (*x* = 2, 2.5, 3, 3.5 h) core/shell nanostructure were confirmed by high-resolution transmission electron microscopy (HRTEM) (Figures S7–S10, Supporting Information). The HRTEM images exhibited clear lattice fringes with an interplanar spacing of 0.234 and 0.198 nm, which agrees well with the (111) and (200) planes of cubic CoO, respectively. The results of element mapping also unambiguously confirmed the hierarchical CuO–CoO core/shell heterostructure. Obviously, the morphology of CoO shell was affected by reaction time (Figure 2c1–f2 and Figures S11–S14 (Supporting Information)). The shell of CuO–CoO-*x* nanostructures was gradually converted from nanosheets into nanoneedles with increasing reaction time. This morphology transformation could be attributed to surface tension-driven curving and scrolling of nanosheets into nanoneedles to reduce the surface energy.[38] Such a scrolling may reduce active area of CuO–CoO nanostructures. As an evidence, the Brunauer–Emmett–Teller (BET) surface area of CuO–CoO-2.5 h (3.9 $m^2\ g^{-1}$) was larger than that of $Cu(OH)_2$ (3.2 $m^2\ g^{-1}$) and other CuO–CoO-*x* composites (Figure S15, Supporting Information). Furthermore, more CoO was deposited with increasing reaction time as seen from TEM energy-dispersive X-ray spectroscopy (TEM–EDS) shown in Figure S16 (Supporting Information). The signal intensity of Co from line-scan TEM–EDS elemental analysis of single CuO–CoO-*x* nanostructure was enhanced gradually (≈50 to ≈220) when reaction time increased from 2 to 3.5 h. Therefore, accompanied by scrolling of CoO nanosheets, overdense packing of CoO shell on CuO would occur for longer reaction time and may hinder the charge transfer to underlying substrate.

As-prepared hierarchical CuO–CoO interface on Cu foam colligated the merits of individual 2D nanostructures and 3D

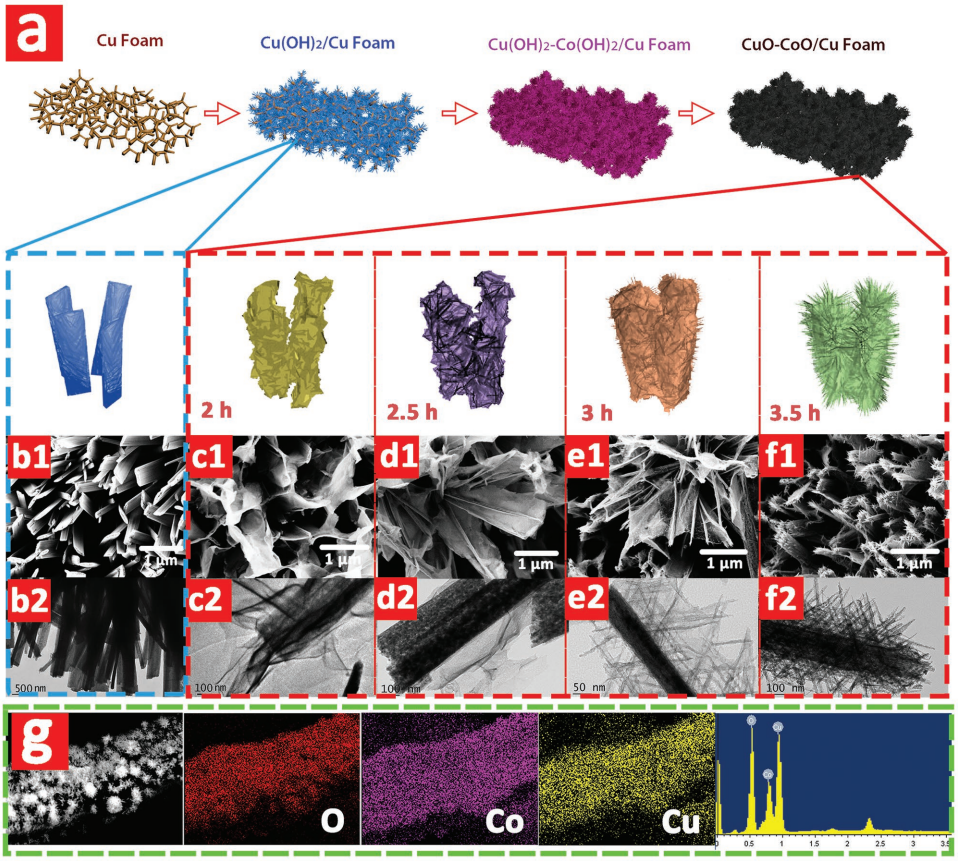


**Figure 2.** a) Schematic illustration of fabrication steps for hybrid CuO–CoO-*x* core/shell heterostructures; Field-emission scanning electron microscope (FESEM) and TEM images of b1,b2) $Cu(OH)_2$, c1,c2) CuO–CoO-2 h, d1,d2) CuO–CoO-2.5 h, e1,e2) CuO–CoO-3 h, and f1,f2) CuO–CoO-3.5 h; g) FESEM–EDS mapping of CuO–CoO-2.5 h sample.

network, which provides abundant active sites and promoted charge transfer.[39] Electrochemical impedance spectroscopy measurement was carried out to probe the interfacial electron transfer properties of the electrodes. Experimental data shown in the form of Nyquist plot in Figure S17a–e (Supporting Information) could be well fitted based on a simplified equivalent circuit model that contained an electrolyte resistance ($R_s$), an interface capacitance (constant-phase-element (CPE)), a charge-transfer resistance ($R_{ct}$), and a Warburg impedance ($Z_w$) (Figure S17f, Supporting Information).[40] The charge-transfer resistance ($R_{ct}$) of CuO–CoO-2.5 h (57 Ω) similar to that of $Cu(OH)_2$ (62 Ω) was significantly lower than $R_{ct}$ of CuO–CoO-2 h (108 Ω), CuO–CoO-3 h (233 Ω), and CuO–CoO-3.5 h (346 Ω). This result demonstrated that leaf-like nanostructure of CuO–CoO-2.5 h with larger surface area provided faster electron transfer kinetics at CuO–CoO/electrolyte interfaces. The promoted interfacial charge transfer is conducive to the electrochemical determination of $H_2O_2$. As for CuO–CoO-3 h and CuO–CoO-3.5 h electrodes, even though more CoO formed at the interface, scrolling and overdense packing of CoO shell as evidenced by TEM observation increased the resistance of charge transfer.

To assess the electrocatalytic activity, bare Cu foam, $Cu(OH)_2$/Cu foam, as well as CuO–CoO-*x*/Cu foam were used as working electrodes for cyclic voltammetry (CV) tests. **Figure 3**a illustrated that the CuO–CoO-2.5 h/Cu foam electrode had a considerable increase of reductive current compared to the other electrodes in 0.1 M phosphate buffer solution (PBS) containing $0.4 \times 10^{-3}$ M $H_2O_2$, verifying the improvement of surface activation and electron-transfer processes. The enhanced electrochemical performance was most probably attributed to unique heterostructure of CuO–CoO-2.5 h. Its leaf-like structure supplied not only effective electronic channels but also amounts of active sites that were helpful to improve the electrochemical detection of $H_2O_2$. Applied potential in chronoamperometry has a significant influence on the sensitivity of an electrochemical sensor.[41] The electrode was further evaluated at different applied potentials. Figure 3b displayed the amperometric response of CuO–CoO-2.5 h electrode upon successive addition of $0.1 \times 10^{-3}$ M $H_2O_2$ at different potentials. The highest current response was presented at –0.5 V. The scan rate ($\nu$)-dependent CV on CuO–CoO-2.5 h electrode in the range of 20–200 mV $s^{-1}$ was investigated in $0.1 \times 10^{-3}$ M $H_2O_2$ solution (Figure 3c). Both anodic and cathodic peak currents ($I$) linearly varied with the square root of the scan rate ($\nu^{1/2}$), suggesting typical diffusion-controlled process (Figure 3d). Figure 3e displayed the CV curves of CuO–CoO-2.5 h electrode in 0.1 M PBS containing different concentrations of $H_2O_2$, and the cathodic peak currents linearly increased with $H_2O_2$ concentration, indicating an excellent electrocatalytic activity of $H_2O_2$ reduction (Figure 3f).

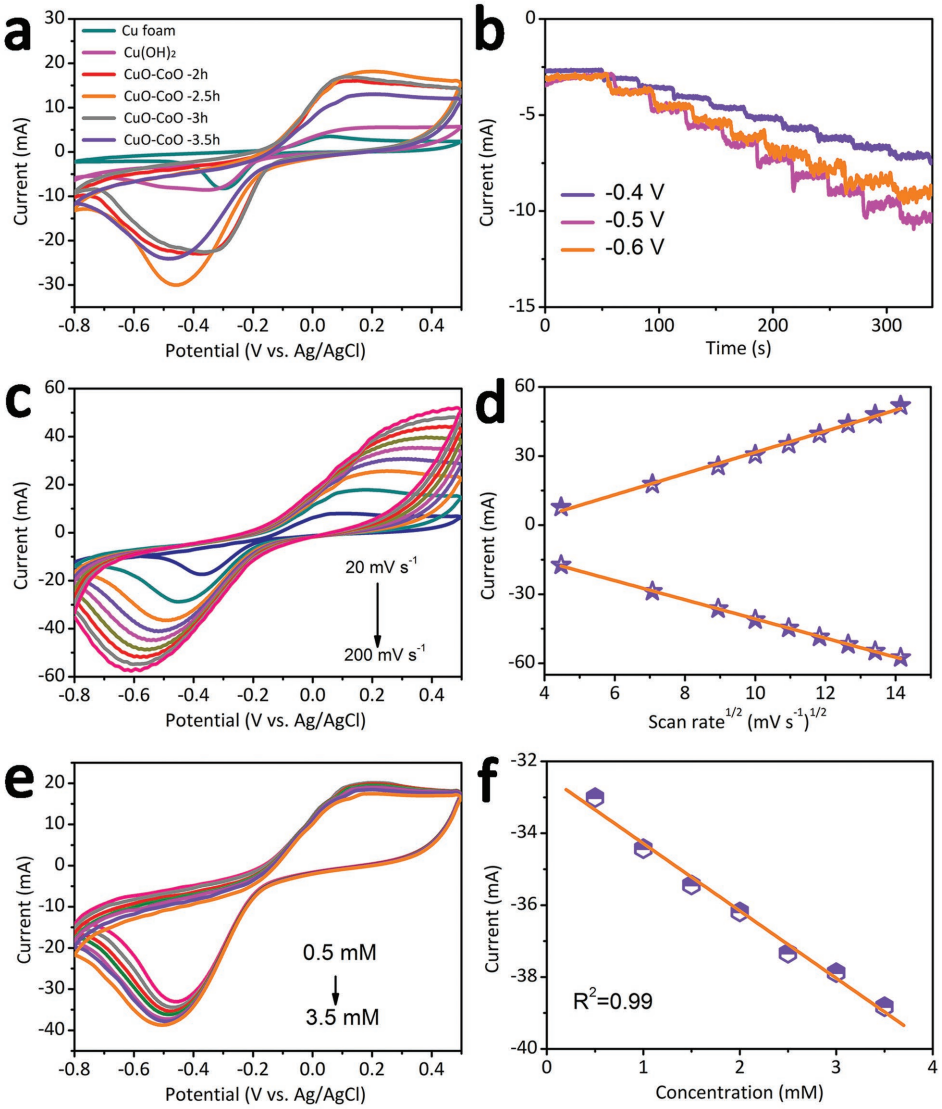


**Figure 3.** a) CVs of various electrodes in 0.1 M PBS (pH 7.4) containing $0.4 \times 10^{-3}$ M $H_2O_2$ at the scan rate of 50 mV $s^{-1}$. b) Amperometric response of CuO–CoO-2.5 h electrode to successive addition of $0.1 \times 10^{-3}$ M $H_2O_2$ at different applied potentials. c) CVs of the CuO–CoO-2.5 h electrode in 0.1 M PBS (pH 7.4) containing $0.1 \times 10^{-3}$ M $H_2O_2$ at different scan rates and d) the plot of oxidation peak current and reduction peak current versus the square root of the scan rate. e) CVs of CuO–CoO-2.5 h electrode in 0.1 M PBS (pH 7.4) containing different concentrations of $H_2O_2$ at the scan rate of 50 mV $s^{-1}$ and f) the relationship between peak currents and $H_2O_2$ concentrations.

**Figure 4**a displayed the current–time curves of as-prepared electrodes in 0.1 M PBS upon successive addition of $0.1 \times 10^{-3}$ M $H_2O_2$ at an applied potential of –0.5 V (vs Ag/AgCl), and the corresponding current–concentration relationship was presented in Figure 4b. Clearly, CuO–CoO-2.5 h electrode showed significant increase in current response compared with the other three CuO–CoO electrodes and the bare copper foam (Figure S18, Supporting Information). This is likely to be a result of enhanced active area and interfacial electron transfer on leaf-like CuO–CoO-2.5 h nanostructures.

Figure 4c showed the amperometric curve of CuO–CoO-2.5 h electrode holding potential at –0.5 V upon continuous addition of $H_2O_2$ with various concentrations into 0.1 M PBS solution. The steady-state current could be achieved within 3 s after $H_2O_2$ was injected, which showed fast adsorption and reduction of $H_2O_2$ on the surface of CuO–CoO-2.5 h material. The inset of Figure 4c presented amperometric response of $H_2O_2$ at low concentrations, indicating a good electrocatalytic ability of the material. Figure 4d displayed the corresponding calibration curve of current versus $H_2O_2$ concentration in a wide linear range from $2 \times 10^{-6}$–$4 \times 10^{-3}$ M with the regression equation of $I$ (mA) = –6.349 ($\times 10^{-3}$ M) – 0.35967 ($R^2 = 0.992$), and the detection limit was estimated to be $1.4 \times 10^{-6}$ M (signal-to-noise ratios (S/N) = 3). The low detection limit could be comparable to previously reported results of Cu-based and Co-based catalysts for determination of $H_2O_2$, but the ultra-high sensitivity (6349 μA m $M^{-1}$ $cm^{-2}$) was super among these catalysts (Tables S1 and S2, Supporting Information). These

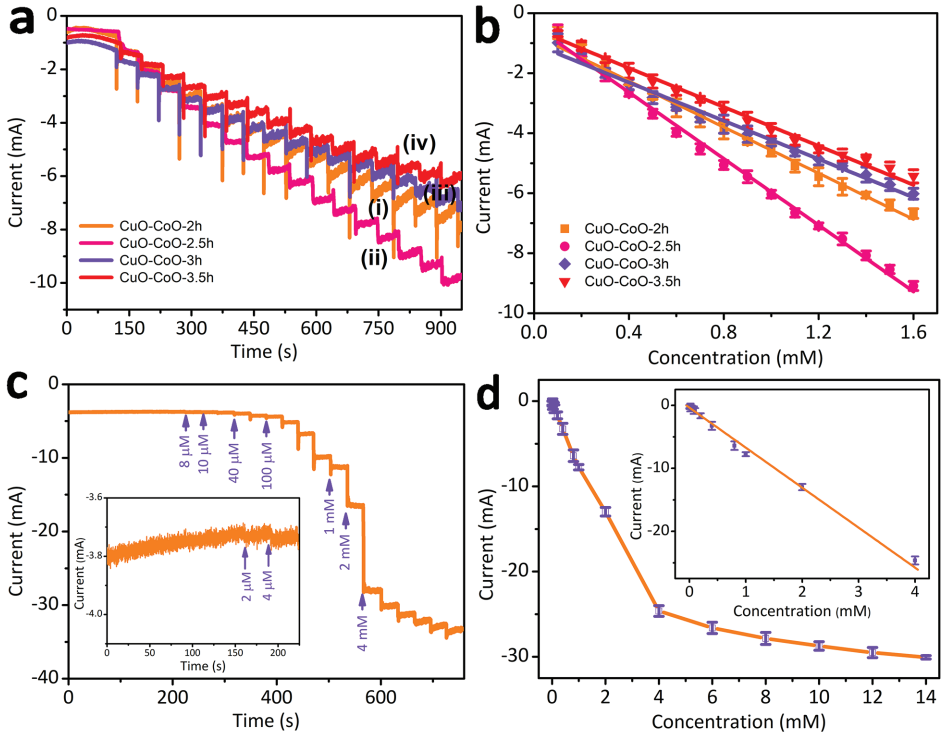


**Figure 4.** a) A steady-state current–time response of i) CuO–CoO-2 h, ii) CuO–CoO-2.5 h, iii) CuO–CoO-3 h, and iv) CuO–CoO-3.5 h electrode upon successive additions of $0.1 \times 10^{-3}$ M $H_2O_2$ in $N_2$-saturated 0.1 M PBS (pH 7.4) at an applied potential of –0.5 V. b) The corresponding calibration curves of CuO–CoO-2 h, CuO–CoO-2.5 h, CuO–CoO-3 h, and CuO–CoO-3.5 h electrodes for the $H_2O_2$ determination. c) Amperometric response of CuO–CoO-2.5 h electrode to dropwise adding $H_2O_2$ into 0.1 M PBS (pH 7.4) at a potential of –0.5 V; Inset: amperometric response of $H_2O_2$ at lower concentration. d) Calibration curve of current versus $H_2O_2$ concentration; Inset: linear calibration curve in the $H_2O_2$ concentration range of $2 \times 10^{-6}$–$4 \times 10^{-3}$ M.

results suggested that the hierarchical leaf-like CuO–CoO heterostructure possessed delicate core–shell interface favorable to surface adsorption and electron transfer for sensitive determination of $H_2O_2$.

According to previous reports,[42–45] the mechanism of $H_2O_2$ reduction in PBS solution was considered as following processes (Equations (1)–(3))

$$H_2O_2 + e^- \leftrightarrow \left(H_2O_2^-\right)_{ads} \quad (1)$$

$$\left(H_2O_2^-\right)_{ads} + e^- \leftrightarrow \left(2HO^-\right)_{ads} \quad (2)$$

$$\left(2HO^-\right)_{ads} + 2H^+ \xleftarrow{\text{FAST}} 2H_2O \quad (3)$$

The mechanism involves a reductive $H_2O_2$ adsorption on the surface of electrode (first step) followed by a reductive dissociation of $H_2O_2$ (second step). Equation (2) is the rate-determining step on account of the fact of the cleavage of O—O bond in the dissociation process. The rate of Equation (1) is related to the surface vacancy sites, while the rate of Equation (2) depends on the adsorption amount of $H_2O_2$ on the surface. In order to further clarify the underlying mechanism of CuO–CoO heterostructure on the catalytic performance toward $H_2O_2$ electroreduction, density functional theory (DFT) calculations on optimized slab models (Figure S19, Supporting Information) were performed.

As shown in **Figure 5**a, CuO–CoO heterostructure also displayed a synergistic effect on decreasing adsorption energy of $H_2O_2$ on CoO (200) shell layer. The adsorption energy was dramatically reduced when thin CoO (200) layer was deposited on CuO surface. **Table 1** exhibited that the surface energy of CuO (111) was comparatively smaller, suggesting that CuO (111) surface was stable. It also showed that CuO (111)-based heterojunction was more stable. When comparing density of states of CoO (111) and CoO (200) at Fermi energy level, it shows that CoO (111) has better transport properties (Figure 5b). However, for CuO–CoO core–shell hetero-nanostructure, CuO/CoO (200) was better in transport properties than CuO/CoO (111) at Fermi energy level, whatever the core was, CuO (111) or CuO (200). It would be expected that CuO/CoO (200) has the best performance for sensing $H_2O_2$. But in CuO–CoO-3 h and CuO–CoO-3.5 h, scrolling of CoO nanosheets notably reduced the active area of CoO (200) layer and deteriorated the electrode performances. Therefore, a fine control of morphology and crystal structure in CuO–CoO-2.5 h was conducive to detect $H_2O_2$.

The capability of recognizing target molecule from interfering substances generally coexisted in a complex biological system is of great concern for a sensor.[46] Chronoamperometry was performed by successively adding $0.1 \times 10^{-3}$ M interfering agents (including NaCl, glucose, fructose, uric acid, dopamine, and ascorbic acid) and $0.1 \times 10^{-4}$ M $H_2O_2$ into 0.1 M PBS. As seen in **Figure 6**a, these interfering species exhibited minimal

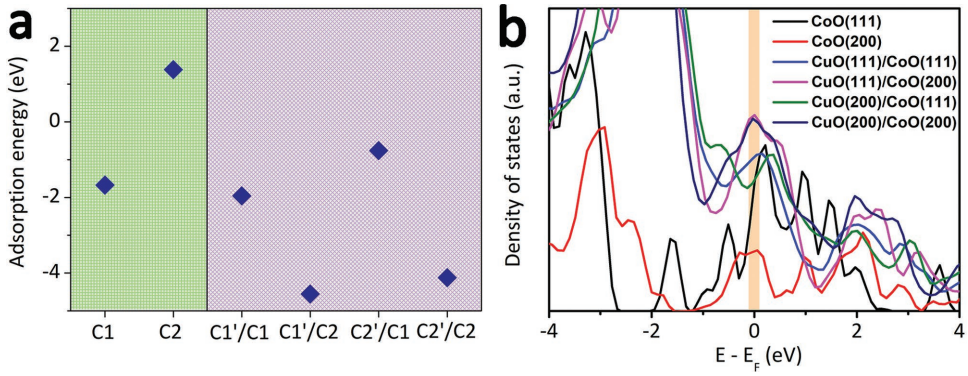


**Figure 5.** a) Adsorption energies of $H_2O_2$ on different CoO, CuO/CoO crystal faces. C1, C2, C1′, C2′, C1′/C1, C1′/C2, C2′/C1, and C2′/C2 represent CoO (111), CoO (200), CuO (111), CuO (200), CuO (111)/CoO (111), CuO (111)/ CoO (200), CuO (200)/CoO (111), and CuO (200)/CoO (200) lattice planes, respectively. b) Total density of states of CoO (111), CoO (200), CuO (111)/CoO (111), CuO (111)/CoO (200), CuO (200)/CoO (111), and CuO (200)/CoO (200) slab models.

response under the applied potential, in contrast to sensitive response of $H_2O_2$, well demonstrating excellent selectivity of the sensor.

Reproducibility and long-time stability of the as-fabricated electrodes were also tested. Four independent electrodes were used for investigating current response to $2 \times 10^{-3}$ M $H_2O_2$, which exhibited a good reproducibility with an acceptable relative standard deviation (RSD) of 2.8% (Figure S20, Supporting Information). Moreover, the long-term stability of CuO–CoO-2.5 h electrodes was evaluated after storing the electrode at 4 °C for two weeks. The current response remained 94% of its initial value that confirmed an excellent stability.

To verify the feasibility of the proposed sensor in the detection of real samples, $H_2O_2$ in apple juice (commercial) and human serum (from the Affiliated Drum Tower Hospital of Nanjing University Medical School) were analyzed using CuO–CoO-2.5 h electrode. The recovery was assessed by spiking $H_2O_2$ with three different concentrations. The results listed in **Table 2** and Figure S21 (Supporting Information) confirmed the recoveries of 99.9–100.7% for apple juice and 99.8–100.5% for serum, and thus suggested potential application of proposed sensor for $H_2O_2$ determination in biological systems.

$H_2O_2$ is one of the major molecules linked with many cell functions and capable as a marker for tumor cells. Chronoamperometry was used to monitor the current response of $H_2O_2$ released from human lung carcinoma cells A549 in real time. Phorbol 12-myristate 13-acetate (PMA) was employed as an external stimulator to induce the cancer cells to release $H_2O_2$ by disrupting their intracellular redox homeostasis.[47] Curve (ii) in Figure 6b was the current response of CuO–CoO-2.5 h electrode in presence of the cancer cells in 0.1 M PBS at an applied potential of −0.5 V. With the addition of PMA, the current response increased, indicating release of $H_2O_2$ from the cells. However, no current increase could be observed when catalase, a selective scavenger of $H_2O_2$, was introduced together with PMA, proving that the current increase was owing to $H_2O_2$ released from the cells. In the control, no obvious signal was observed (curve (i)) upon addition of PMA or catalase without cell suspension. These results demonstrated that the designed sensor could be used to monitor extracellular ROS and has potential in biochemical, physiological, and pathological investigations.[48]

## 3. Conclusion

In summary, we have developed core–shell nanoarchitectures of CoO nanosheets growth on CuO nanoplates by a facile chemical bath deposition process for the electrochemical detection of $H_2O_2$. By controlling reaction time, the morphology and nanostructure of the hybrids can be conveniently modulated. Leaf-like CuO–CoO-2.5 h with favorable interface structure can significantly improve electrocatalytic activity. The rationally designed nanostructure with unique surface configuration presented synergistic effects that enhanced $H_2O_2$ adsorption and interfacial electron transfer. These advantages endow the proposed sensor ultrahigh sensitivity, low detection limit, good selectivity, and wide detection range for $H_2O_2$. Furthermore, CuO–CoO-2.5 h-based sensor presented good potential for monitoring $H_2O_2$ in real samples and cellular $H_2O_2$ release in real time. Thus, this hybrid material provides an effective strategy for developing promising nonenzyme $H_2O_2$ biosensor.

## 4. Experimental Section

*Preparation of Copper Hydroxide on Copper Foam*: Solution for synthesis of $Cu(OH)_2$ was prepared by mixing 8 mL of 10 M NaOH, 4 mL of 1 M $(NH_4)_2S_2O_8$, 4 mL of $NH_3 \cdot H_2O$, and 40 mL of deionized water. Two pieces of clean copper foam (2 cm × 1 cm) were immersed into the

**Table 1.** Surface energies of CoO, CuO, CuO/CoO slab models.

| Materials | CuO | | CoO | | CuO/CoO | | | |
|---|---|---|---|---|---|---|---|---|
| *hkl* | 111 | 200 | 111 | 200 | 111/111 | 111/200 | 200/111 | 200/200 |
| Surface energies [J $m^{-2}$] | 0.22 | 0.80 | 2.27 | 2.27 | 3.90 | 3.33 | 5.22 | 5.80 |

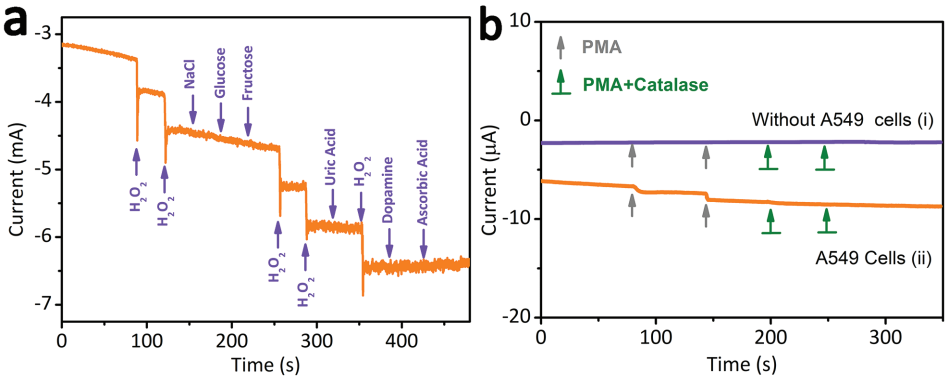


**Figure 6.** a) Amperometric response of CuO–CoO-2.5 h electrode upon addition of $0.1 \times 10^{-4}$ M $H_2O_2$, $0.1 \times 10^{-3}$ M NaCl, $0.1 \times 10^{-3}$ M glucose, $0.1 \times 10^{-3}$ M fructose, $0.1 \times 10^{-3}$ M uric acid, $0.1 \times 10^{-3}$ M dopamine, and $0.1 \times 10^{-3}$ M ascorbic acid to 0.1 M phosphate buffer solutions (pH 7.4). b) Amperometric response of the CuO–CoO-2.5 h electrode i) without and ii) with A549 cells upon sequential addition of PMA and catalase at different intervals.

above solution for 45 min at room temperature, and then washed with water and ethanol. The as-prepared $Cu(OH)_2$/Cu foam was obtained after dried under vacuum conditions for 24 h at 50 °C.

*Preparation of CuO–CoO Samples*: To synthesize CuO–CoO catalysts, a precursor solution was first prepared by dissolving urea and cobalt salts ($CoSO_4 \cdot 7H_2O$, molar ratio urea:Co = 15:1) in 150 mL deionized water. Then, previously prepared $Cu(OH)_2$/Cu foam was placed in well-mixed precursor solution, and sealed with aluminum foil, kept at 85 °C for 2–3.5 h. After cooled to ambient temperature, the foam was washed with water and ethanol for three times, dried at 50 °C, and calcined at 350 °C in nitrogen for 2 h. Samples were denoted as CuO–CoO-*x* (*x* is the reaction time).

*Detection of $H_2O_2$ Released from Living Cells*: Human lung carcinoma cells A549 were cultured in a Dulbecco's modified Eagle medium (high glucose, Gibco) containing 10% fetal bovine serum in a humidified atmosphere with 5% $CO_2$ at 37 °C. Cells were digested with 0.25 wt% trypsin at 37 °C for 120 s and separated from the culture medium by centrifugation at 1000 rpm for 10 min, then washed with PBS (0.1 M, pH 7.4) for three times. A pellet that contained 105 cells was resuspended into 3 mL PBS solution. PMA was employed as the stimulant for $H_2O_2$ release.

*Theoretical Calculations*: All calculations were performed by using the Vienna Ab initio Simulation Package.[49,50] The exchange correlation potential was described by the Perdew–Burke–Ernzerhof functional-based generalized gradient approximation.[51] The projector augmented wave method[52,53] was applied for the electron–ion interactions and the cutoff energy was 500 eV. In the DFT + *U* method, a Hubbard *U* term was used to avoid the self-interaction error and *U* value for Co 3d was chosen as 6.88 eV.[54] Cubic CoO (space group: $Fm\bar{3}m$) with 8 atoms was calculated and monoclinic CuO (space group: *C*2/*c*) with 8 atoms was calculated. We used $3 \times 3 \times 3$ K-point mesh when calculating bulk CuO and CoO and $3 \times 3 \times 1$ K-point mesh for slab model. The (111) and (200) surfaces of CoO and CuO were chosen and calculated. Vacuum thickness of 20 Å was chosen to simulate the surface properties.

**Table 2.** Determination of $H_2O_2$ in real sample.

| Real samples | Added [$\times 10^{-6}$ M] | Detected [$\times 10^{-6}$ M] | Recovery [%] | RSD [%] |
|---|---|---|---|---|
| Apple juice | 30.0 | 30.2 | 100.7 | 2.8 |
| | 150.0 | 149.9 | 99.9 | 4.1 |
| | 300.0 | 300.5 | 100.2 | 1.3 |
| Serum | 150.0 | 149.7 | 99.8 | 2.5 |
| | 500.0 | 502.4 | 100.5 | 3.6 |
| | 1000.0 | 998.2 | 99.8 | 2.7 |

## Supporting Information

Supporting Information is available from the Wiley Online Library or from the author.

## Acknowledgements

This work was supported by the National Science Foundation of China (NSFC no. 51172043).

## Conflict of Interest

The authors declare no conflict of interest.

## Keywords

CuO–CoO, $H_2O_2$, heterostructures, nonenzymatic biosensors

Received: October 24, 2017
Revised: January 18, 2018
Published online:

[1] J. Tang, Y. Quan, Y. Zhang, M. Jiang, A. M. Al-Enizi, B. Kong, T. An, W. Wang, L. Xia, X. Gong, *Nanoscale* **2016**, *8*, 5786.
[2] Y. Liu, X. Liu, Z. Guo, Z. Hu, Z. Xue, X. Lu, *Biosens. Bioelectron.* **2017**, *87*, 101.
[3] L. Kong, Z. Ren, N. Zheng, S. Du, J. Wu, J. Tang, H. Fu, *Nano Res.* **2015**, *8*, 469.
[4] H. Dai, W. Lü, X. Zuo, Q. Zhu, C. Pan, X. Niu, J. Liu, H. Chen, X. Chen, *Biosens. Bioelectron.* **2017**, *95*, 131.
[5] F. Pagliari, C. Mandoli, G. Forte, E. Magnani, S. Pagliari, G. Nardone, S. Licoccia, M. Minieri, P. Di Nardo, E. Traversa, *ACS Nano* **2012**, *6*, 3767.
[6] P. Wu, Z. Cai, Y. Gao, H. Zhang, C. Cai, *Chem. Commun.* **2011**, *47*, 11327.
[7] J. Xi, C. Xie, Y. Zhang, L. Wang, J. Xiao, X. Duan, J. Ren, F. Xiao, S. Wang, *ACS Appl. Mater. Interfaces* **2016**, *8*, 22563.
[8] Y. Zhang, C. Wu, X. Zhou, X. Wu, Y. Yang, H. Wu, S. Guo, J. Zhang, *Nanoscale* **2013**, *5*, 1816.
[9] N. Akhtar, S. A. El-Safty, M. Khairy, W. El-Said, *Sens. Actuators, B* **2015**, *207*, 158.

[10] N. Yusoff, P. Rameshkumar, M. S. Mehmood, A. Pandikumar, H. W. Lee, N. M. Huang, *Biosens. Bioelectron.* **2017**, *87*, 1020.
[11] M. Hara-Chikuma, H. Satooka, S. Watanabe, T. Honda, Y. Miyachi, T. Watanabe, A. Verkman, *Nat. Commun.* **2015**, *6*, 7454.
[12] F. Wen, Y. Dong, L. Feng, S. Wang, S. Zhang, X. Zhang, *Anal. Chem.* **2011**, *83*, 1193.
[13] S. Du, Z. Ren, J. Wu, W. Xi, H. Fu, *Nano Res.* **2016**, *9*, 2260.
[14] J. Xi, Y. Zhang, N. Wang, L. Wang, Z. Zhang, F. Xiao, S. Wang, *ACS Appl. Mater. Interfaces* **2015**, *7*, 5583.
[15] S. Chakraborty, C. R. Raj, *Biosens. Bioelectron.* **2009**, *24*, 3264.
[16] J. Yuan, K. Wang, X. Xia, *Adv. Funct. Mater.* **2005**, *15*, 803.
[17] J. Bai, X. Jiang, *Anal. Chem.* **2013**, *85*, 8095.
[18] W. Zhang, G. Jia, Z. Li, C. Yuan, Y. Bai, D. Fu, *Adv. Mater. Interfaces* **2017**, *4*, 1601241.
[19] Z. Wang, X. Cao, D. Liu, S. Hao, R. Kong, G. Du, A. M. Asiri, X. Sun, *Chem. - Eur. J.* **2017**, *23*, 4986.
[20] K. Zhao, X. Yan, Y. Gu, Z. Kang, Z. Bai, S. Cao, Y. Liu, X. Zhang, Y. Zhang, *Small* **2016**, *12*, 245.
[21] S. Chen, R. Yuan, Y. Chai, F. Hu, *Microchim. Acta* **2013**, *180*, 15.
[22] D. Zhou, X. Q. Cao, Z. Wang, S. Hao, X. D. Hou, F. L. Qu, G. Du, A. M. Asiri, C. B. Zheng, X. P. Sun, *Chem. - Eur. J.* **2017**, *23*, 5214.
[23] Y. Cao, Y. Yang, Y. Shan, Z. Huang, *ACS Appl. Mater. Interfaces* **2016**, *8*, 5998.
[24] M. H. Sun, S. Z. Huang, L. H. Chen, Y. Li, X. Y. Yang, Z. Y. Yuan, B. L. Su, *Chem. Soc. Rev.* **2016**, *45*, 3479.
[25] D. Seliktar, *Science* **2012**, *336*, 1124.
[26] G. Gao, H. B. Wu, S. Ding, X. W. D. Lou, *Small* **2015**, *11*, 432.
[27] W. Qiu, M. Xu, R. Li, X. Liu, M. Zhang, *Anal. Chem.* **2016**, *88*, 1117.
[28] H. Jiang, P. S. Lee, C. Li, *Energy Environ. Sci.* **2013**, *6*, 41.
[29] R. Kumar, R. K. Singh, P. K. Dubey, D. P. Singh, R. M. Yadav, *ACS Appl. Mater. Interfaces* **2015**, *7*, 15042.
[30] L. Dai, S. Mo, Q. Qin, X. Zhao, N. Zheng, *Small* **2016**, *12*, 1572.
[31] J. Yang, T. Zhou, R. Zhu, X. Chen, Z. Guo, J. Fan, H. K. Liu, W. X. Zhang, *Adv. Mater. Interfaces* **2016**, *3*, 1500464.
[32] Y. Yang, X. Yang, Y. Tan, Q. Yuan, *Nano Res.* **2017**, *10*, 1560.
[33] S. Chakraborty, W. Hong, K. J. Endres, T. Z. Xie, L. Wojtas, C. N. Moorefield, C. Wesdemiotis, G. R. Newkome, *J. Am. Chem. Soc.* **2017**, *139*, 3012.
[34] Y. Wang, J. Tang, T. Zhou, P. Da, J. Li, B. Kong, Z. Yang, G. Zheng, *Small* **2014**, *10*, 4967.
[35] J. Wang, Q. Zhang, X. Li, B. Zhang, L. Mai, K. Zhang, *Nano Energy* **2015**, *12*, 437.
[36] Q. Zhang, K. Zhang, D. Xu, G. Yang, H. Huang, F. Nie, C. Liu, S. Yang, *Prog. Mater. Sci.* **2014**, *60*, 208.
[37] S. Xiong, J. S. Chen, X. W. Lou, H. C. Zeng, *Adv. Funct. Mater.* **2012**, *22*, 861.
[38] J. Yu, Q. Li, J. Fan, B. Cheng, *Chem. Commun.* **2011**, *47*, 9161.
[39] J. Romo-Herrera, M. Terrones, H. Terrones, S. Dag, V. Meunier, *Nano Lett.* **2007**, *7*, 570.
[40] J. L. Shi, W. C. Du, Y. X. Yin, Y. G. Guo, L. J. Wan, *J. Mater. Chem. A* **2014**, *2*, 10830.
[41] Q. Wang, Y. Yang, F. Gao, J. Ni, Y. Zhang, Z. Lin, *ACS Appl. Mater. Interfaces* **2016**, *8*, 32477.
[42] C. Zhang, L. Li, J. Ju, W. Chen, *Electrochim. Acta* **2016**, *210*, 181.
[43] W. Zhao, H. Wang, X. Qin, X. Wang, Z. Zhao, Z. Miao, L. Chen, M. Shan, Y. Fang, Q. Chen, *Talanta* **2009**, *80*, 1029.
[44] C. Gomez, A. Silva, M. Strumia, L. Avalle, M. Rojas, *Nanoscale* **2017**, *9*, 11170.
[45] G. Luque, M. Rojas, G. Rivas, E. Leiva, *Electrochim. Acta* **2010**, *56*, 523.
[46] Z. Kang, X. Yan, Y. Wang, Y. Zhao, Z. Bai, Y. Liu, K. Zhao, S. Cao, Y. Zhang, *Nano Res.* **2016**, *9*, 344.
[47] H. R. Zhang, Y. Z. Wang, W. Zhao, J. J. Xu, H. Y. Chen, *Anal. Chem.* **2016**, *88*, 2884.
[48] M. H. Naveen, N. G. Gurudatt, H. B. Noh, Y. B. Shim, *Adv. Funct. Mater.* **2016**, *26*, 1590.
[49] G. Kresse, J. Furthmüller, *Phys. Rev. B* **1996**, *54*, 11169.
[50] G. Kresse, J. Furthmüller, *Comput. Mater. Sci.* **1996**, *6*, 15.
[51] J. P. Perdew, K. Burke, M. Ernzerhof, *Phys. Rev. Lett.* **1996**, *77*, 3865.
[52] P. E. Blöchl, *Phys. Rev. B* **1994**, *50*, 17953.
[53] G. Kresse, D. Joubert, *Phys. Rev. B* **1999**, *59*, 1758.
[54] F. Tran, P. Blaha, K. Schwarz, P. Novák, *Phys. Rev. B* **2006**, *74*, 155108.